Preliminary Investigation Into the Effects of Cross-Flow on Low Reynolds Number Transition

Alejandra Uranga[*]

Massachusetts Institute of Technology, Cambridge, MA 02139, U.S.A.

Per-Olof Persson[†]

University of California Berkeley, Berkeley, CA 94720 U.S.A.

Mark Drela[‡] and Jaime Peraire[§]

Massachusetts Institute of Technology, Cambridge, MA 02139, U.S.A.

The present work presents a preliminary investigation into the effects of cross-flow on transition at low Reynolds numbers, an area which has essentially remained unexplored. The flow around an infinite SD7003 wing at an angle of attack of $4°$ is considered at a chord Reynolds numbers of 60,000, and for sweep angles ranging between $0°$ and $60°$. A separation bubble is present on the upper surface where the flow transitions to turbulence, and both Tollmien-Schlichting (TS) waves and cross-flow instabilities are observed.

The level of coupling between cross-flow and streamwise boundary layer velocity components is evaluated by projecting them along two-dimensional equivalent directions. It is established that the cross-flow *cannot* be decoupled from the streamwise evolution for sweep angles between about $10°$ and $40°$ due to strong non-linear interactions that take place after the laminar boundary layer separates. Hence, in separation-induced transition at low Reynolds numbers, it is not possible to treat streamwise and cross-flow instabilities independently for wings at intermediate sweep angles, and predicting the mixed transition cannot be reduced to treating the disturbances of each component separately. Furthermore, the type of transition (TS dominated, cross-flow dominated, or mixed) is *a priori* unknown, as soon as the flow is slightly misaligned with the wing's chord—an important presumption for the study of unsteady flows encountered in MAVs and animal locomotion.

I.   Introduction

THE low Reynolds number regime has been the subject of growing interest in the last decades, a consequence of both advancements in Micro-Air Vehicles (MAVs) and studies of animal locomotion—swimming of fish, flying of birds and bats, flapping of insects. In the simulation of such flows with characteristic Reynolds numbers between roughly 10^3 and 10^4, accurately predicting transition to turbulence is of crucial importance since the transition location has a significant impact on aerodynamic performance. This is linked to the fact that laminar flows have a much greater tendency to separate than the essentially turbulent flows encountered at high Reynolds numbers. When a laminar boundary layer separates in an adverse pressure gradient, triggering transition and reattachment, it forms what is known as a laminar separation bubble (LSB).

The present works advances the understanding of low Reynolds number transition in an LSB. Building upon our previous studies of the flow around a straight wing,[1–3] the focus is now on transition along a swept wing in order to study the effect that a cross-flow velocity component in the boundary layer has on flow

---

[*]Postdoctoral Associate, Dept. of Aeronautics and Astronautics, 77 Massachusetts Avenue Room 37-442, Cambridge, MA 02139, auranga@mit.edu, AIAA Member.
[†]Assistant Professor, Department of Mathematics, AIAA Member.
[‡]Terry J. Kohler Professor of Fluid Dynamics, Dept. of Aeronautics and Astronautics, AIAA Fellow.
[§]Professor, Dept. of Aeronautics and Astronautics, AIAA Associate Fellow.

American Institute of Aeronautics and Astronautics

stability and transition. While cross-flow transition has been the subject of a large number of studies in high Reynolds number flows, it has remained essentially unexplored at low Reynolds numbers.

Simulation of transition requires low numerical dispersion and dissipation, and therefore the use of high-order methods seems to be a practical requirement. A high-order Discontinuous Galerkin (DG) Finite Element method is used as it combines high accuracy with the geometric flexibility required for practical applications. The computational methodology and boundary layer analysis employed in the present work are the same that we had used to study the flow around an infinite straight wing at different Reynolds numbers.[2,3] Those results proved the advantages of this approach by providing a good comparison with both experimental and better-resolved simulations published by other groups. Furthermore, Tollmien-Schlichting waves were observed, their growth quantified, and the transition mechanism demonstrated.

As previously, an infinite SD7003 rectangular wing section is set at an angle of attack of $4°$, a characteristic case exhibiting an LSB on the upper surface for a range of flow conditions. The Reynolds numbers based on chord is set at 60,000 and the free-stream flow angle with respect to the leading-edge line is varied in order to represent the flow over a wing at different sweep angles.

II.   Background

The nature of cross-flow over swept wings at large Reynolds number is explained in the works by Reed and Roshotko.[4–6] Near the leading edge, the combination of pressure gradient and sweep deflects the inviscid streamlines inward (*i.e.* away from the tip of a backwards-sweep wing), and then outwards near the trailing edge. The boundary layer flow carries less momentum and hence this deflection is larger near the wall, which results in a secondary flow perpendicular to the inviscid streamline direction, known as cross-flow. Hence, the cross-flow velocity is zero both at the boundary layer edge and at the wall, such that the cross-flow profile has an inflection point and is inviscidly unstable. Disturbances in the form of cross-flow vortices propagate, which rotate around an axis oriented close to the inviscid streamline direction and have a span-wise periodicity of the same order as the boundary layer thickness (about twice or three times the thickness).

The parameters which are important in cross-flow stability studies are the height of the inflection point (related to inviscid stability), the velocity gradient at this point (with larger shear stresses resulting in more unstable profiles), and the maximum cross-flow velocity (linked to the streamline curvature inducing it).

A finding which is of particular importance to transition prediction at high Reynolds numbers is the following: when the cross-flow is unstable, the boundary layer stability characteristics are very close to those of the cross-flow alone (*i.e.* irrespective of the streamwise flow); when the cross-flow is stable, the stability characteristics are essentially those of the streamwise profile. Hence, the stability of the cross-flow and streamwise profiles can usually be considered separately.[6,7]

As Reed & Saric[5] point out, cross-flow instability is usually dominant near the leading edge where pressure gradients are important, and the shift between cross-flow and streamwise (Tolmien-Schlichting) instability occurs when the cross-flow profiles become S-shaped and hence highly stable. The authors note that in the region where the prevalent mechanism switches, e^N envelope methods need to be used carefully and critical factors for transition due to cross-flow instability can be very large. Furthermore, non-linear saturation of disturbance amplitude can be observed before transition, and methods based on linear stability are inappropriate to predict cross-flow dominated transition.[5,8,9]

Another important consideration is that, due to the large streamwise velocity gradients close to the wall and the related substantial momentum exchanges, small fluctuations in cross-flow or in normal velocity can lead to large steam-wise disturbances which soon become too large for non-linear interactions to be neglected.[9] This can occur even close to the attachment line which divides the flow between the branch that follows the upper surface and the one that follows the lower surface. Thus, a flow can transition due to the growth of streamwise instabilities over swept wings and yet be destabilized by cross-flow fluctuations.

Before the present work, and to the author's knowledge, the possible decoupling of cross-flow and stream-wise amplification had not been studied for low Reynolds number transition, and it remained unknown whether the conclusions for high Reynolds number flows were still applicable. We introduce here a systematic approach to assessing the level of coupling between streamwise and cross-flow components, and show how non-linear coupling is significant when intermediate levels of cross-flow are present.

American Institute of Aeronautics and Astronautics

III.   Computational Methodology

The present section provides a description of the computational approach used for solving the three-dimensional, unsteady, compressible Navier-Stokes equations with the Discontinuous Galerkin method. Details on the time-stepping procedure and computational grids are given, followed by an explanation of how the different sweep angles are simulated. Finally, we explain how the boundary layer is analyzed and the transition mechanism established. Most of this section is common to our previously published study of low Reynolds number transition over an infinite SD7003 un-swept wing.[2,3]

A.   High-Order Discontinuous Galerkin Method

The unsteady, compressible Navier-Stokes equations are solved using a high-order Discontinuous Galerkin method implemented in the computational code *3DG*. This framework solves time-dependent systems of conservation laws of the form

$$\begin{cases} \dfrac{\partial \mathbf{u}}{\partial t} + \nabla \cdot \mathbf{F}^{(i)}(\mathbf{u}) - \nabla \cdot \mathbf{F}^{(v)}(\mathbf{u}, \mathbf{q}) = \mathbf{S}(\mathbf{u}, \mathbf{q}) \\ \mathbf{q} - \nabla \mathbf{u} = 0 \end{cases} \tag{1}$$

in a domain Ω, with conserved state variables $\mathbf{u}$, inviscid flux function $\mathbf{F}^{(i)}$, viscous flux function $\mathbf{F}^{(v)}$, and source term $\mathbf{S}$.

In the case of the three-dimensional, unsteady, compressible Navier-Stokes equations,

$$\mathbf{u} = \begin{bmatrix} \rho \\ \rho u_1 \\ \rho u_2 \\ \rho u_3 \\ \rho E \end{bmatrix}, \quad \mathbf{F}_i^{(i)} = \begin{bmatrix} \rho u_i \\ \rho u_i u_1 + \delta_{i1} p \\ \rho u_i u_2 + \delta_{i2} p \\ \rho u_i u_3 + \delta_{i3} p \\ \rho u_i (E + p/\rho) \end{bmatrix}, \quad \mathbf{F}_i^{(v)} = \begin{bmatrix} 0 \\ \tau_{i1} \\ \tau_{i2} \\ \tau_{i3} \\ u_k \tau_{ik} + \frac{\mu \gamma}{Pr} \frac{\partial e}{\partial x_i} \end{bmatrix}, \quad \mathbf{S} = \begin{bmatrix} 0 \\ 0 \\ 0 \\ 0 \\ 0 \end{bmatrix}. \tag{2}$$

In the above equations, $e = E - u_k u_k / 2$ is the internal energy per unit mass, ρ denotes the fluid density, u_i the velocity component in the direction x_i, p the static pressure, E the total energy per unit mass, μ the dynamic viscosity coefficient, and Pr the flow Prandtl number. The viscous stress tensor, τ_{ij}, and the heat flux, q_i, are defined by

$$\tau_{ij} \equiv \mu \left[\left(\frac{\partial u_i}{\partial x_j} + \frac{\partial u_j}{\partial x_i} \right) - \frac{2}{3} \frac{\partial u_k}{\partial x_k} \delta_{ij} \right] \tag{3}$$

$$q_j = -\frac{\mu}{Pr} \frac{\partial}{\partial x_j} \left(E + \frac{p}{\rho} - \frac{1}{2} u_k u_k \right) . \tag{4}$$

In order to close the system, the ideal gas equation of state is used in its form

$$p = (\gamma - 1) \rho \left(E - \frac{1}{2} u_k u_k \right) . \tag{5}$$

The specific heat ratio is set to $\gamma = 1.4$ and the Prandtl number to $Pr = 0.72$. Moreover, the kinematic viscosity, $\nu = \mu / \rho$, is assumed to be constant since only low Mach number flows are considered.

Following the finite element procedure, we consider a triangulation $\mathcal{T}_h$ of the spatial domain Ω and introduce the finite element spaces

$$\begin{aligned} V_h &= \{ v \in [L^2(\Omega)]^m \mid v|_K \in [\mathcal{P}_p(K)]^m, \ \forall K \in \mathcal{T}_h \}, \\ \Sigma_h &= \{ r \in [L^2(\Omega)]^{dm} \mid r|_K \in [\mathcal{P}_p(K)]^{dm}, \ \forall K \in \mathcal{T}_h \}, \end{aligned}$$

where $\mathcal{P}_p(K)$ is the space of polynomial functions of degree at most $p \geq 1$ on the tetrahedral element K, m is the dimension of $\mathbf{u}$ and number of states, and d is the spatial dimension. In the case of three-dimensional simulations, $d = 3$ and $m = 5$. Curved elements are handled by iso-parametric mapping to a straight master (reference) element in which the polynomials are defined.

American Institute of Aeronautics and Astronautics

The DG formulation is then of the form: find $\mathbf{u}_h \in V_h$ and $\mathbf{q}_h \in \Sigma_h$ such that for all $K \in \mathcal{T}_h$,

$$\int_K \mathbf{q}_h \cdot \mathbf{r}\, dx = -\int_K \mathbf{u}_h \nabla \cdot \mathbf{r}\, dx + \int_{\partial K} \hat{\mathbf{u}}\, \mathbf{r} \cdot \mathbf{n}\, ds \qquad \forall \mathbf{r} \in [\mathcal{P}_p(K)]^{dm} \ ,$$

$$\int_K \frac{\partial \mathbf{u}_h}{\partial t}\mathbf{v}\, dx - \int_K [\mathbf{F}^{(i)}(\mathbf{u}_h) - \mathbf{F}^{(v)}(\mathbf{u}_h, \mathbf{q}_h)] \cdot \nabla \mathbf{v}\, dx$$

$$= \int_K \mathbf{S}(\mathbf{u}_h, \mathbf{q}_h)\mathbf{v}\, dx - \int_{\partial K} [\hat{\mathbf{F}}^{(i)} - \hat{\mathbf{F}}^{(v)}] \cdot \mathbf{n}\, \mathbf{v}\, ds \qquad \forall \mathbf{v} \in [\mathcal{P}_p(K)]^m \ .$$

Here, the numerical fluxes $\hat{\mathbf{F}}^{(i)}$, $\hat{\mathbf{F}}^{(v)}$ and $\hat{\mathbf{u}}$ are approximations to $\mathbf{F}^{(i)}$, $\mathbf{F}^{(v)}$ and $\mathbf{u}$, respectively, on the boundary ∂K of the element K. The DG formulation is complete once these numerical fluxes are specified in terms of $\mathbf{q}_h$ and $\mathbf{u}_h$, and the boundary conditions set.

The inviscid flux $\hat{\mathbf{F}}^{(i)}$ is determined using Roe's scheme[10] and provides the numerical dissipation needed for ILES. The viscous flux $\hat{\mathbf{F}}^{(v)}$ is calculated using the Compact Discontinuous Galerkin (CDG) method:[11] by choosing the numerical flux $\hat{\mathbf{u}}$ to be a function of $\mathbf{u}_h$ and not $\mathbf{q}_h$, the additional $\mathbf{q}_h$ variables can be eliminated after discretization at element level. This results in a system involving only the degrees of freedom corresponding to the conserved variables $\mathbf{u}_h$. The final result is a system of coupled ordinary differential equations of the form

$$\boldsymbol{M}\dot{\boldsymbol{u}} = \boldsymbol{R}(\boldsymbol{u}) \ , \tag{6}$$

where $\boldsymbol{u}$ is a vector containing the degrees of freedom associated with $\mathbf{u}_h$, and $\dot{\boldsymbol{u}}$ denotes its time derivative. Here, $\boldsymbol{M}$ is the mass matrix and $\boldsymbol{R}$ is the residual vector which is a nonlinear function of $\boldsymbol{u}$. Nodal basis expansions are used to represent $\mathbf{u}_h$ inside each element.

The system (6) is linearized using Newton's method and the resulting linear system solved using the Conjugate Gradient Squared (CGS) method preconditioned by incomplete factorizations (ILU) following Persson & Peraire 2008.[12] The code is parallelized using a domain-decomposition approach with block-wise ILU factorizations, the details of which can be found in the paper by Persson 2009.[13]

In the present work we follow the Implicit Large Eddy Simulation (ILES) approach, and the unresolved small eddies are accounted for by means of the numerical dissipation. Hence, no subgrid-scale model is employed and the full (unfiltered) compressible Navier-Stokes equations are solved. This approach was used successfully for the simulation of low Reynolds number flows around an SD7003 airfoil in our previously published studies,[2, 3] and also by Visbal and collaborators using a sixth-order compact difference method.[14–17]
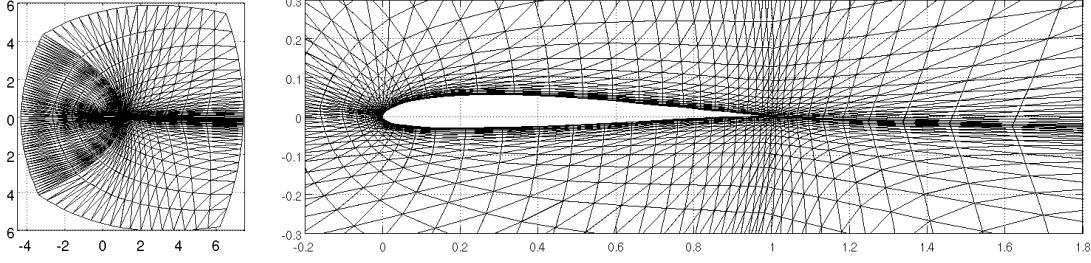
B.   Computational Domain and Grid

The flow around a rectangular wing with an SD7003 airfoil profile at an angle of attack of $4°$ and free-stream Mach number of 0.2 is considered. The axes are set with x being the chord-wise direction and z the span-wise direction, such that the leading-edge is located along the line $x = 0$, $y = 0$.

From the wing's leading-edge line, the domain extends 4.3 chord lengths upstream, 7.4 chord lengths downstream, 5.9 chord lengths above, and 6.0 chord lengths below. The wing span-to-chord ratio is set to 0.2 chords following previously published results.[2, 3, 14] Thus, if we denote by c the chord length, the domain has the range $[-4.3c\ , 7.4c] \times [-6.0c\ , 5.9c] \times [0\ , 0.2c]$ along the chord-wise, vertical, and span-wise directions, respectively.

The computational domain has periodic boundary conditions along the span-wise direction in order to simulate an infinite wing. The wing's surface is represented by a non-slip, adiabatic, boundary condition, while a free-stream type boundary condition employing Roe's approximate Riemann solver is imposed at the outer edges (far-field) of the computational domain.

We use the term *high-order nodes* to refer to all the nodes used in the numerical procedure at which the variable states are computed, so as to differentiate them from the nodes at the corners of each tetrahedral element. Note that the number of high-order nodes is equal to the number of degrees-of-freedom per state.

The grid is constructed by extruding a two-dimensional structured C-mesh around the profile which is generated from a rectangular grid by conformal transformations. To obtain curved elements that are aligned with the geometry boundaries and do not intersect, a fine structured grid is generated and the high-order nodes of the computational mesh placed at the mesh points of this fine grid. Note that this fine grid is such that the number of subdivisions in each direction is compatible with the number of high-order nodes required for a given polynomial order. The tetrahedral connectivities of the computational mesh are then

American Institute of Aeronautics and Astronautics

Figure 1. Span-wise view of the computational grids used in the present preliminary study: (left) domain, (right) closer view on foil.

obtained directly from the cartesian topology of the fine structured grid by splitting each cartesian cell into six tetrahedrals. The boundaries are thus represented accurately and a high-order mesh appropriate for DG computations obtained.

In this preliminary assessment, only one grid is used. In our previous study of unswept wings,[2] the resolution of this grid (called grid 2) in the span-wise y-plane was found to be appropriate to capture the separation bubble and observe the linear growth of unstable waves, even though a higher resolution is needed to accurately predict the locations of separation, transition, and reattachment. The focus here is on how the cross-flow influences transition and on the trends with varying sweep angle. These are not expected to be qualitatively modified as long as the spatial resolution is close to adequate. Simulations with finer meshes are under way and the results presented here will be updated in a future publication.

Third-order polynomials ($p = 3$) are employed for a fourth-order accurate method in space. Figure 1 shows the grid in a planar cut along the span-wise direction (y-plane). It has a total of 158,400 elements, and hence 3,168,000 high-order nodes at $p = 3$. Along the leading-edge line (y direction), there are 12 elements for a total number of unique high-order span-wise nodes of 37. On the airfoil's upper surface, there are 108 unique high-order nodes.

C. Time Stepping and Averaging Procedure

Time stepping is performed with a two-stage, A-stable, third-order accurate diagonal implicit Runge-Kutta (DIRK) method.[18] This allows to take large time steps chosen based on physical time accuracy considerations and not on numerical stability factors. Unless otherwise specified, the simulations are performed with a non-dimensional time step of $dt^* = dt \times U_\infty/c = 0.01$, and the solution is saved every 5 steps for computing statistics and other post-processing tasks ($\Delta t^* = 0.05$).

For all the cases considered, the flow is initialized to a uniform field with the far-field conditions. The initial transient is over by $t^* = 15$ as estimated from the temporal evolution of the forces on the wing. Hence, unless otherwise specified, the average fields, turbulence correlations, and statistics are computed by averaging the solution over a non-dimensional time interval of 10 corresponding to 200 solutions with $t^* \in [15, 25]$, and then performing a spatial average over 20 span-wise planes (unless otherwise specified) since the domain has periodic boundary conditions in the span-wise direction.

D. Visualization of Vortical Structures: Q-Criterion

Vortical coherent structures are identified using the q-criterion[19] and defined as

$$q \equiv \frac{1}{2} \left(\Omega_{ij} \Omega_{ij} - S_{ij} S_{ij} \right) , \tag{7}$$

where Ω_{ij} and S_{ij} are the anti-symmetric and symmetric parts of the velocity gradient, respectively, that is

$$\Omega_{ij} \equiv \frac{1}{2} \left(\frac{\partial u_i}{\partial x_j} - \frac{\partial u_j}{\partial x_i} \right) \quad \text{and} \quad S_{ij} \equiv \frac{1}{2} \left(\frac{\partial u_i}{\partial x_j} + \frac{\partial u_j}{\partial x_i} \right) .$$

In this work iso-surfaces of positive q are used to visualize vortical structures, with the velocity gradients computed consistently with the DG method (*i.e.* using the variables $\mathbf{q}$) to preserve the order of accuracy.

E.   Simulation of Different Sweep Angles

A rectangular, infinite, SD7003 wing is used with a free-stream velocity that has a non-zero component in the direction of the leading edge line in order to simulate a swept wing. With x and y the chord-wise and span-wise directions respectively, the velocity imposed at the farfield of the domain is given by

$$\vec{U}_\infty = \begin{bmatrix} \cos\alpha \\ \tan\Lambda \\ \sin\alpha \end{bmatrix} \tag{8}$$

in which α is the angle of attack, and Λ is the sweep angle which is defined here as the angle between the free-stream velocity and the x-z plane on which the SD7003 foil lies. Note that the angle of attack is the angle between the free-stream velocity and the SD7003 chord (x-direction), that is $\alpha = \tan^{-1}(U_{\infty_z}/U_{\infty_x})$ and is thus consistent with our previous un-swept wing studies.[2,3] The free-stream velocity magnitude is

$$U_\infty = \sqrt{1 + \tan^2\Lambda} = \frac{1}{\cos\Lambda} \ .$$

In order to keep the descriptions consistent with those in the absence of cross-flow, the term *chord-wise* is used to refer to the x-direction which preserves the SD7003 geometry, while the foil that the free-stream flow sees is the SD7003 scaled by a factor of $\sqrt{1 + \tan^2\Lambda}$ along its chord as illustrated in Figure 2. Similarly, *span-wise* refers to the direction of the leading edge line, that is the y-direction.

The chord-wise Reynolds number, Re_x, thus refers to the Reynolds number in the direction normal to the leading edge line, and is kept at $Re_x = 60{,}000$. In this way, the flow in the chord-wise direction should be similar at all sweep angles except for the non-linar coupling between the cross-flow and the streamwise components as explained in Section F. The effects of cross-flow on the boundary layer development and transition to turbulence can thus be assessed by comparing the results with different values of Λ. Note that the free-stream Reynolds number, $Re_\infty = Re_x\sqrt{1 + \tan^2\Lambda} = Re_x/\cos\Lambda$, and the span-wise Reynolds number, $Re_y = Re_x\tan\Lambda$, vary with sweep angle.

Furthermore, the pressure and skin friction forces are non-dimensionalized with respect to the dynamic pressure projected along the chord-wise direction in order to obtain pressure and friction coefficients which allow for a meaningful comparison. The forces are thus divided by $q_{\infty_x} = {}^1\!/_2\,\rho\,U_{\infty_x}^2$ instead of the usual $q_\infty = {}^1\!/_2\,\rho\,U_\infty^2$; this corresponds to a factor of $(1 + \tan^2\Lambda)$. The coefficients of lift (force component normal to the free-stream direction) and drag (force in the free-stream direction) are referred to as C_L and C_D, respectively, while $C_{L_x} = C_L(1 + \tan^2\Lambda)$ and $C_{D_x} = C_D(1 + \tan^2\Lambda)$ denote the chord-wise lift and drag coefficients, respectively, which are relative to q_{∞_x}.

The arbitrary sign choice implied by the definition of the cross-flow unit vector $\hat{s}_2 = \hat{s}_1 \times \hat{n}$ (see Section G), results in a dominantly negative cross-flow. In order to avoid confusion, we refer to the average profile $-\overline{u}_2/\overline{u}_e$ as the *cross-flow pseudo-velocity profile* or simply as the *cross-flow velocity*.
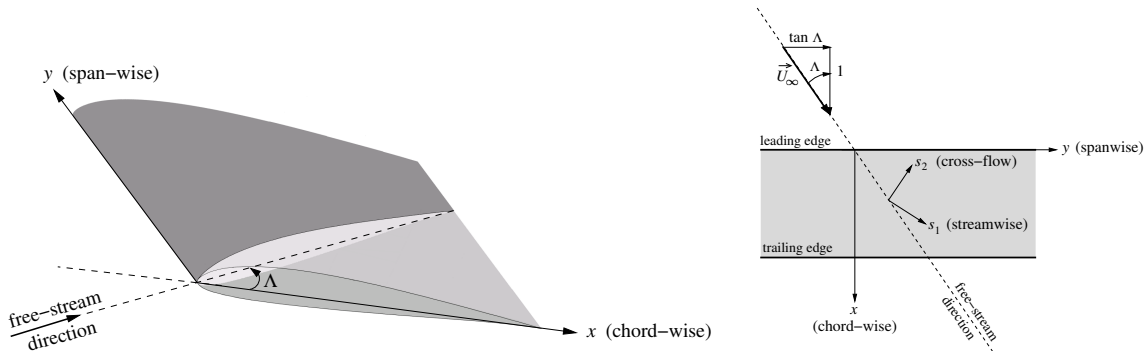

Figure 2. Illustration of the free-stream velocity $\vec{U}_\infty$, chord-wise direction x, and span-wise direction y for the swept-wing flow; Λ is the sweep angle.

American Institute of Aeronautics and Astronautics

F.   Swept-Wing Theory for Laminar Flow

Let us consider the Navier-Stokes equations for a three-dimensional, steady, incompressible, laminar flow whose velocity vector has components u in the chord-wise x direction, v in the span-wise y direction, and w in the transverse z direction. It is reasonable to assume that the changes along the span-wise direction over a constant-chord swept-wing are much smaller than changes that occur along both the chord-wise and the transverse directions. This is a good approximation not only for small sweep angles, but for any sweep provided that one is far away from the wing ends (which is always the case for an infinite wing). The y-derivative terms ($\partial/\partial y$) can thus be neglected in front of x and z derivatives, and the governing equations simplified to

$$\frac{\partial u}{\partial x} + \frac{\partial w}{\partial z} = 0$$
$$u\frac{\partial u}{\partial x} + w\frac{\partial u}{\partial z} = -\frac{1}{\rho}\frac{\partial p}{\partial x} + \nu\left(\frac{\partial^2 u}{\partial x^2} + \frac{\partial^2 u}{\partial z^2}\right)$$
$$u\frac{\partial v}{\partial x} + w\frac{\partial v}{\partial z} = \nu\left(\frac{\partial^2 v}{\partial x^2} + \frac{\partial^2 v}{\partial z^2}\right)$$
$$u\frac{\partial w}{\partial x} + w\frac{\partial w}{\partial z} = -\frac{1}{\rho}\frac{\partial p}{\partial z} + \nu\left(\frac{\partial^2 w}{\partial x^2} + \frac{\partial^2 w}{\partial z^2}\right) \ .$$

An interesting property of a flow governed by the above equations is that the components u and w are decoupled from v, but v depends on u and w. To make this clear consider the first, second, and last equations above, namely

$$\begin{cases} \dfrac{\partial u}{\partial x} + \dfrac{\partial w}{\partial y} = 0 \\[2mm] u\dfrac{\partial u}{\partial x} + w\dfrac{\partial u}{\partial z} = -\dfrac{1}{\rho}\dfrac{\partial p}{\partial x} + \nu\left(\dfrac{\partial^2 u}{\partial x^2} + \dfrac{\partial^2 u}{\partial z^2}\right) \\[2mm] u\dfrac{\partial w}{\partial x} + w\dfrac{\partial w}{\partial z} = -\dfrac{1}{\rho}\dfrac{\partial p}{\partial z} + \nu\left(\dfrac{\partial^2 w}{\partial x^2} + \dfrac{\partial^2 w}{\partial z^2}\right) \end{cases} \tag{9}$$

This system can be solved for u, w, p (three equations, three unknown functions of x and z), irrespective of the span-wise velocity: it predicts the two-dimensional laminar boundary layer flow on the airfoil's plane. The additional equation

$$u\frac{\partial v}{\partial x} + w\frac{\partial v}{\partial z} = \nu\left(\frac{\partial^2 v}{\partial x^2} + \frac{\partial^2 v}{\partial z^2}\right) \tag{10}$$

defines v at given u and w. Hence, there is a one-way coupling between the laminar flow component in the span-wise direction and the components on the chord-wise plane: v depends on u and w, but the converse is not true.

Comparing the chord-wise boundary layer flow at different sweep angles thus allows to study the influence (if any) of the cross-flow present over swept wings on the boundary layer development and transition. The above analysis predicts no influence in the laminar boundary layer region; on the other hand, turbulence is a highly non-linear process which could be responsible for a two-way coupling in which the span-wise flow influences the chord-wise boundary layer evolution.

G.   Boundary Layer Analysis

In order to compute the boundary layer integral quantities, we first obtain the pseudo-velocity profile by integrating the flow vorticity, namely

$$\vec{u}^*(x,n) = \int_0^n \vec{\omega} \times \hat{n}\, dn \ . \tag{11}$$

Here $\vec{u}^*$ denotes the pseudo-velocity, $\vec{\omega}$ the flow vorticity vector, $\hat{n}$ the unit vector normal to the airfoil at the location considered, and n the local coordinate along $\hat{n}$. The reason for using this pseudo-velocity profile is that it always asymptotes outside the boundary layer, even with strong curvature, thus making the edge of the boundary layer a well defined location.

American Institute of Aeronautics and Astronautics

The edge n_e of the boundary layer is then taken to be the location where *both* the magnitudes of vorticity, $|\vec{\omega}|$, and of vorticity's normal variation, $|\partial\vec{\omega}/\partial n|$, are below a certain threshold, namely

$$\begin{cases} |\vec{\omega}|\, n < \epsilon_0 |\vec{u}^*| , \\ \left|\dfrac{d\vec{\omega}}{dn}\right| n^2 < \epsilon_1 |\vec{u}^*| . \end{cases} \tag{12}$$

The edge velocity is then $\vec{u}_e^* = \vec{u}^*(n_e)$, and has magnitude $u_e = |\vec{u}_e^*|$. The values $\epsilon_0 = 0.01$ and $\epsilon_1 = 0.1$ were found to allow for a robust and systematic detection of the boundary layer edge for the simulations reported in the present work.

Local streamwise and cross-flow unit vectors are then defined as, respectively,

$$\hat{s}_1 = \vec{u}_e^*/u_e \quad \text{and} \quad \hat{s}_2 = \hat{s}_1 \times \hat{n} . \tag{13}$$

Thus, the streamwise and cross-flow velocity profiles are given by, respectively,

$$u_1(x, n) = \vec{u}^*(x, n) \cdot \hat{s}_1 \quad \text{and} \quad u_2(x, n) = \vec{u}^*(x, n) \cdot \hat{s}_2 . \tag{14}$$

The boundary layer streamwise displacement and momentum thicknesses are then

$$\delta_1^* = \int_0^{n_e} \left(1 - \frac{u_1}{u_e}\right) dn \tag{15}$$

$$\theta_{11} = \int_0^{n_e} \left(1 - \frac{u_1}{u_e}\right) \frac{u_1}{u_e} \, dn , \tag{16}$$

and the streamwise shape factor is

$$H_{11} = \delta_1^*/\theta_{11} . \tag{17}$$

Note that the boundary layer analysis relies on quantities at points along lines normal to the foil's surface. These are obtained by interpolating within the grid's tetrahedral elements in a manner consistent with the order of the polynomials being used in order to preserve the accuracy of the method. Moreover, as many stations along the foil (or the chord) are employed as there are unique grid nodes, and about 100 points inside the boundary layer along the normal are taken.

The cross-flow displacement thickness corresponds to the defect of cross-flow velocity ratio in the boundary layer relative to its edge value which is zero — since the cross-flow vanishes at the boundary layer edge by construction. Hence it is defined as

$$\delta_2^* = \int_0^{n_e} \left(0 - \frac{u_2}{u_e}\right) dn .$$

The momentum thickness is a tensor with four components

$$\theta_{11} = \int_0^{n_e} \left(1 - \frac{u_1}{u_e}\right) \frac{u_1}{u_e} \, dn \quad , \quad \theta_{12} = \int_0^{n_e} \left(1 - \frac{u_1}{u_e}\right) \frac{u_2}{u_e} \, dn \quad ,$$

$$\theta_{21} = \int_0^{n_e} \left(0 - \frac{u_2}{u_e}\right) \frac{u_1}{u_e} \, dn \quad , \quad \theta_{22} = \int_0^{n_e} \left(0 - \frac{u_2}{u_e}\right) \frac{u_2}{u_e} \, dn .$$

Note that, on average, the cross-flow pseudo-velocity u_2 is negative over most of the boundary layer, and hence all the thicknesses δ_i^*, θ_{ij} are positive values except for θ_{12}. These integral quantities defined in the local streamwise, cross-flow reference frame are linked to the sweep angle.

In order to decouple any linear effects, it is useful to consider the chord-wise quantities

$$\delta_x^* = \int_0^{n_e} \left(\frac{u_{e_x}}{u_e} - \frac{u_x^*}{u_e}\right) dn , \tag{18}$$

$$\theta_{xx} = \int_0^{n_e} \left(\frac{u_{e_x}}{u_e} - \frac{u_x^*}{u_e}\right) \frac{u_x^*}{u_e} \, dn , \tag{19}$$

in which u_x^* is the component of the pseudo-velocity $\vec{u}^*$ in the chord-wise x direction. Using the same notation the displacement and momentum thicknesses in a two-dimensional boundary layer are written as

$$\delta^* = \int_0^{n_e} \left(1 - \frac{u_x^*}{u_{e_x}}\right) dn ,$$

$$\theta = \int_0^{n_e} \left(1 - \frac{u_x^*}{u_{e_x}}\right) \frac{u_x^*}{u_{e_x}} dn .$$

A meaningful comparison of the average boundary layer integral quantities can thus be obtained by considering the *two-dimensional equivalent* displacement thickness, momentum thickness, and shape factor for any given sweep angle and at any chord-wise location through the relations

$$\delta^* = \frac{u_e}{u_{e_x}} \delta_x^* , \tag{20}$$

$$\theta = \left(\frac{u_e}{u_{e_x}}\right)^2 \theta_{xx} , \tag{21}$$

$$H = \frac{\delta^*}{\theta} , \tag{22}$$

in which the ratio u_e/u_{e_x} (the inverse of the x component of the streamwise unit vector $\hat{s}_1$) accounts for the effect of sweep on the boundary layer development: it is unity for $\Lambda = 0°$, and increases as the sweep angle increases. The effect of the cross-flow on the chord-wise boundary layer can thus be assessed by comparing the two-dimensional equivalents δ^*, θ, and H for various sweep angles, as done in Section V.

H. Transition Mechanism

In order to identify which mechanism is responsible for transition to turbulence, we compute the fluctuating streamwise pseudo-velocity

$$u_1'(\vec{x}, t) = u_1(\vec{x}, t) - \overline{u}_1(x) ,$$

in which the over-line denotes a temporal average. The increase in perturbation amplitude of disturbances along the chord-wise direction is then quantified by computing the amplification A_1 of streamwise perturbations at any location x along the chord, that is

$$A_1(x) = \frac{1}{\overline{u}_e(x)\sqrt{n_e(x)}} \sqrt{\int_0^{n_e} \overline{u_1'}^2 \, dn} . \tag{23}$$

The amplification factor N_1 of the streamwise perturbations is then

$$N_1(x) = \ln\left(\frac{A_1(x)}{A_{1_0}}\right) , \tag{24}$$

in which A_{1_0} is the amplification at the onset of transition, or equivalently

$$e^{N_1} = \frac{A_1(x)}{A_{1_0}} .$$

Similarly, the amplification of cross-flow instabilities can be assessed by computing

$$A_2(x) = \frac{1}{\overline{u}_e(x)\sqrt{n_e(x)}} \sqrt{\int_0^{n_e} \overline{u_2'}^2 \, dn} \tag{25}$$

to which corresponds the cross-flow amplification factor

$$N_2(x) = \ln\left(\frac{A_2(x)}{A_{2_0}}\right) . \tag{26}$$

American Institute of Aeronautics and Astronautics

IV. Results at $30°$ Sweep Angle

The flow around a wing with sweep angle $\Lambda = 30°$ is now considered in detail. After determining that a span domain length of $0.2c$ is sufficient to capture the mean flow features, the average results are compared with those of the equivalent un-swept ($\Lambda = 0°$) wing.

A. Effect of Domain Span Length

Previous studies over SD7003 un-swept wings[2, 3, 20] determined that a domain length of 0.2 chords in the span-wise direction with periodic boundary conditions is sufficient to simulate an infinite wing. However, the presence of a span-wise velocity component may change the characteristic span-wise length of the flow structures, and hence the flow for a domain with $0.2c$ span is compared to that for a $0.3c$ domain span.

Figure 3 shows the time evolution of lift, drag, and span-wise force coefficients for both cases: the average coefficients differ by less than a quarter of a percent for lift and drag, and by less than 2% for the third component. The forces are similar, Figure 4 shows the pressure and skin friction coefficients and Figure 5 the boundary layer integral parameters of the average flow on the wing. The average pressure and skin forces are undistinguishable, and the small difference in boundary layer quantities after transition can be attributed to a lack of statistical convergence of the time-average flow and not to the difference in the domain's span. Hence, a domain with a span length of $0.2c$ and span-wise periodic boundary conditions is adequate to capture the mean flow features of an infinite wing even with a span-wise free-stream component corresponding to $\Lambda = 30°$.

This span should be adequate for any other sweep angle: for larger sweep angles, the span-wise extent of any flow structures is more likely to decrease than increase; and for smaller Λ, this domain span should be enough since it was found sufficient at $\Lambda = 0$ in our previous studies.[2, 3]
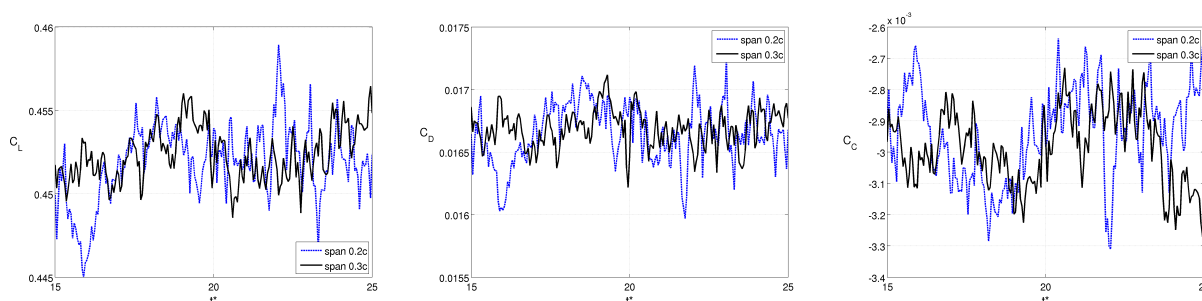
Figure 3. Time variation of lift (top left), drag (top right), and span-wise (bottom) force coefficients for $30°$ sweep wing at $Re_x = 60,000$: comparison of grids with two different span lengths.
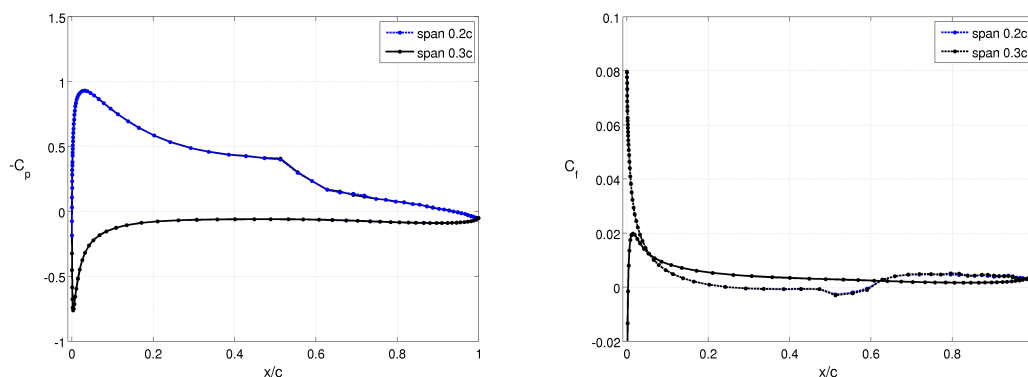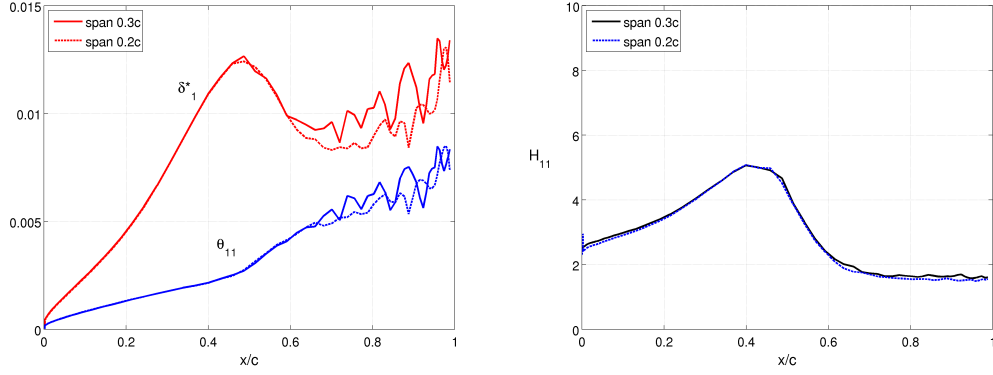

Figure 4. Average pressure coefficient (left) and chord-wise skin friction coefficient (right) for $30°$ sweep wing at $Re_x = 60,000$: comparison of grids with two different span lengths.

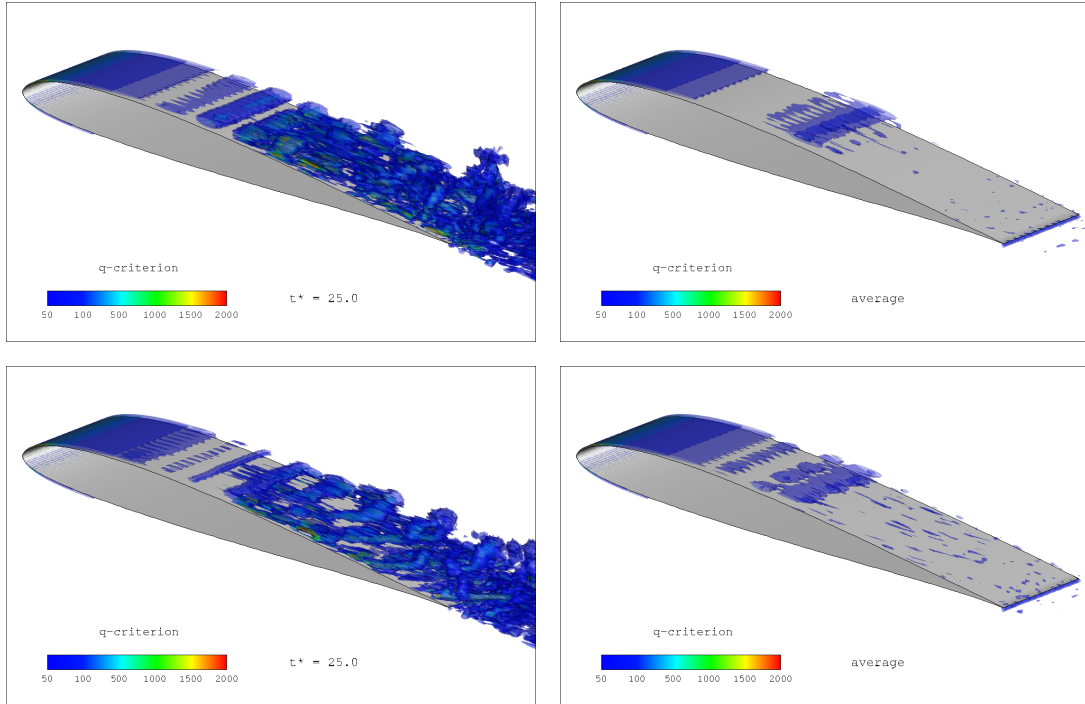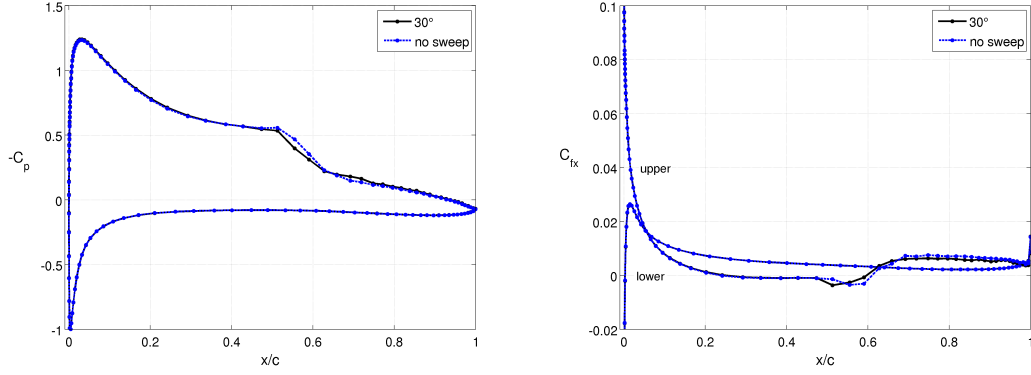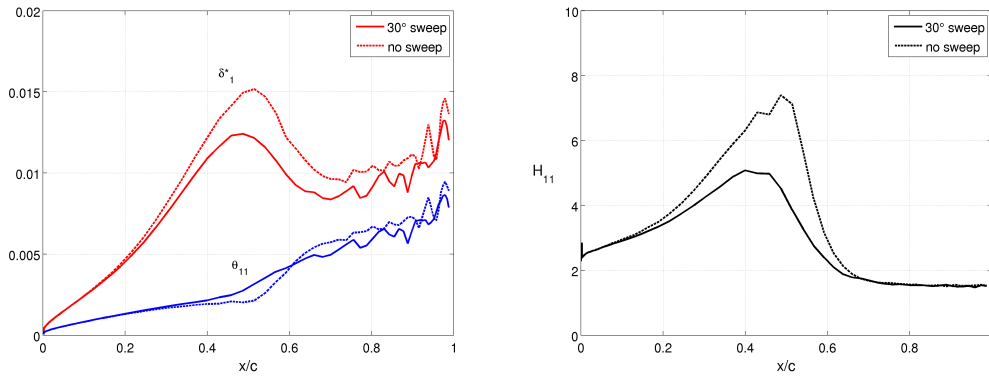American Institute of Aeronautics and Astronautics

Figure 5. Boundary layer average streamwise displacement and momentum thicknesses (left), and shape factor (right) evolution along the chord-wise direction for $30°$ sweep wing at $Re_x = 60,000$: comparison of grids with two different span lengths.

B. Comparison with Un-Swept Wing

The average iso-surfaces of q-criterion of Figure 6 show that the swept wing generates more vortical structures, in particular around the quarter-chord point, than the un-swept wing; this is consistent with the fact that the flow becomes unstable earlier. Note that the noise in the average iso-surfaces on the downstream half of the swept wing indicate that more time averaging is needed due to the presence of smaller, higher-frequency structures over the swept wing.

Figure 7 shows the pressure and chord-wise skin friction coefficients for both $\Lambda = 0$ (un-swept wing, no cross-flow) and $\Lambda = 30°$. As mentioned previously, non-dimensionalization of pressure and skin friction forces is done with respect to the free-stream dynamic pressure projected along the chord-wise direction, q_{∞_x}, which is the same for all values of Λ since $Re_x = 60,000$ is kept constant.

Figure 6. Instantaneous (left) and average (right) iso-surfaces of q-criterion for un-swept wing (top) and wing with $30°$ sweep (bottom) at $Re_x = 60,000$.

Figure 7. Average pressure coefficient (left) and chord-wise skin friction coefficient (right): comparison of un-swept and $30°$ sweep wing at $Re_x = 60,000$.

Figure 8. Boundary layer average streamwise displacement and momentum thicknesses (left), and shape factor (right) evolution along the chord-wise direction: comparison of un-swept and $30°$ sweep wing at $Re_x = 60,000$.

1. Boundary Layer

Figure 8 provides a comparison of the boundary layer streamwise displacement thickness, momentum thickness, and shape factor for straight and swept wing. Separation and transition locations are taken at the locations where the shape factor H_{11} reaches 4 and where it peaks, respectively. The separation location does not change significantly (5% farther downstream for the swept wing), but transition does occur significantly earlier (18%) in the presence of cross-flow. This, and the considerations that follow, shows that the presence of a cross-flow component destabilizes the streamwise velocity profile.

The average and fluctuating profiles of streamwise pseudo-velocity at different chord-wise locations for $\Lambda = 30°$ of Figure 9 are qualitatively similar to those without cross-flow. The streamwise profile at $x/c = 0.1$ with and without sweep can be seen in Figure 10: the difference, though very small, is largest on the half of the boundary layer thickness close to the wall where shear stress is important.

The cross-flow pseudo-velocity profiles, $-\overline{u}_2/\overline{u}_e$, of Figure 11 show the profile which vanishes both at the wall and at the boundary layer edge. Moreover, the cross-flow has an S-shaped profile with two inflection points when close to the wing's leading edge: the cross-flow velocity $-\overline{u}_2/\overline{u}_e$ goes from being positive near the wall (*i.e.* cross-flow directed towards the root of a wing with backward sweep), to negative near the boundary layer edge before asymptoting to zero at the edge. Downstream of $x/c \approx 0.13$, the cross-flow velocity remains of the same sign (positive) all the way from the wall up to the boundary layer edge. Thus, the cross-flow velocity direction is consistent with the description given in Section II where the cross-flow near the leading edge is described to be directed towards the root on a wing with positive sweep.

A quantitative measure of how much cross-flow is present is given by the value of the maximum average cross-flow, $\max(-\overline{u}_2/\overline{u}_e)$, along the chord-wise direction shown on the left plot of Figure 12: the black line indicates that the maximum cross-flow increases linearly as we move downstream up to the transition location of $x_{tr}/c = 0.3996$, while the dotted blue line shows that the location of maximum cross-flow moves
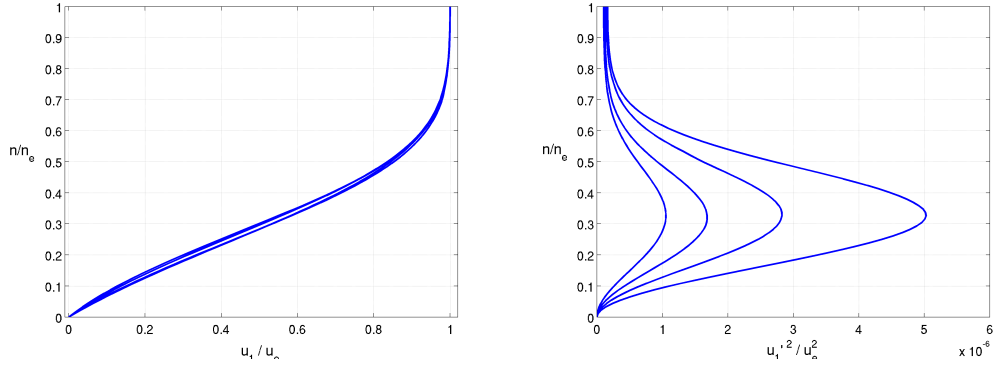
Figure 9. Boundary layer average profiles of streamwise pseudo-velocity $\overline{u}_1/\overline{u_e}$ (left), and fluctuating streamwise pseudo-velocity $\overline{u_1'^2}/\overline{u_e^2}$ (right), at different chord-wise locations $x/c \in [0.1, 0.15]$ for $30°$ sweep wing at $Re_x = 60,000$.
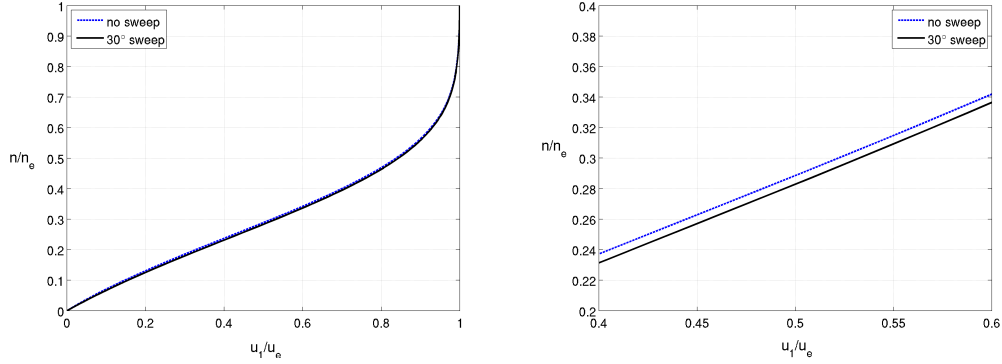

Figure 10. Boundary layer average streamwise profile $\overline{u}_1/\overline{u_e}$ at $x/c = 0.1$: comparison of un-swept and $30°$ sweep wing at $Re_x = 60,000$.
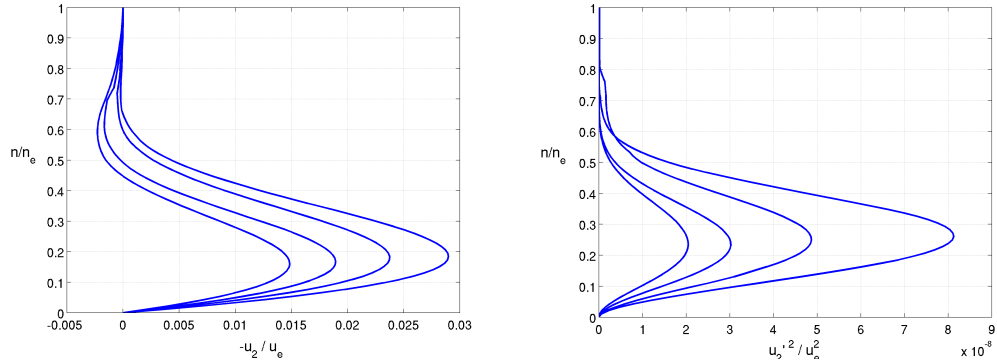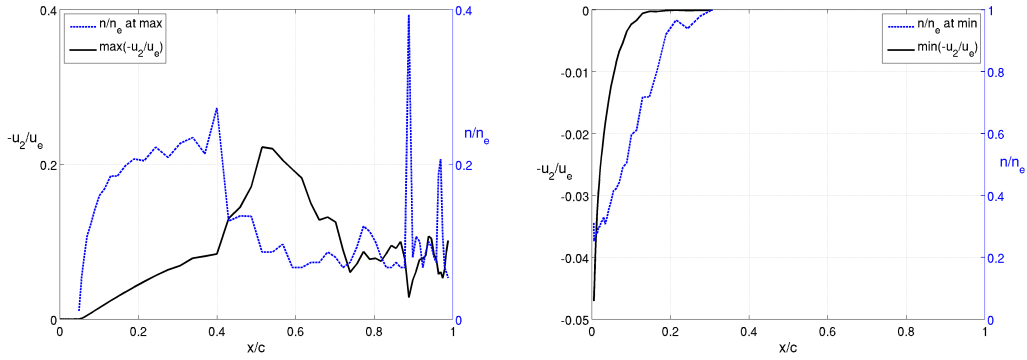

Figure 11. Boundary layer average profiles of cross-flow pseudo-velocity $-\overline{u}_2/\overline{u_e}$ (left), and fluctuating cross-flow pseudo-velocity $\overline{u_2'^2}/\overline{u_e^2}$ (right), at different chord-wise locations $x/c \in [0.1, 0.15]$ for $30°$ sweep wing at $Re_x = 60,000$.

American Institute of Aeronautics and Astronautics

Figure 12. Values and locations of maximum (left) and minimum (right) average cross-flow velocity $-\overline{u}_2/\overline{u}_e$
for $30°$ **sweep wing and** $Re_x = 60,000.$

away from the wall as we move downstream down towards transition. The large variations past transition can probably be explained, again, by the need for computing time averages over more steps.

The right-hand-side of Figure 12 shows how the value of the minimum cross-flow velocity (the local extrema near the boundary layer edge which gives the cross-flow profile an S-shape) increases as we move downstream, and eventually becomes zero thus leaving a cross-flow profile with a single inflection point. Furthermore, as this happens, the locus of minimum negative cross-flow moves closer and closer to the boundary layer edge as indicated by the dotted blue line.

2. Amplification of Disturbances

A comparison of streamwise amplification factor, N_1, evolution between the wing without cross-flow and the wing at $\Lambda = 30°$ can be seen in Figure 13. As expected and as confirmed by the earlier occurrence transition, the amplification factor grows faster in the presence of cross-flow (slope of 16 in the region of linear increase where disturbances grow exponentially) than for the un-swept wing (linear slope of 13).

However, the streamwise profiles with and without sweep only differ slightly as can be seen in Figure 10. If one solves the Orr-Sommerfeld equation for both of these profiles, the resulting growth factors differ by only 3%, thus proving that the change in streamwise profiles is insignificant from a stability point of view. As explained in the background section, the cross-flow/TS interaction is particularly important since the cross-flow velocity magnitude is significant near the wall (highest at around 20% of the boundary layer thickness) which is a region of high shear where the streamwise profile has a large gradient. Thus, even more than modifying the streamwise profile, the presence of a cross-flow velocity modifies the stability of the overall flow: the transition over the $30°$ swept wing is not anymore solely caused by the growth of TS waves, but is
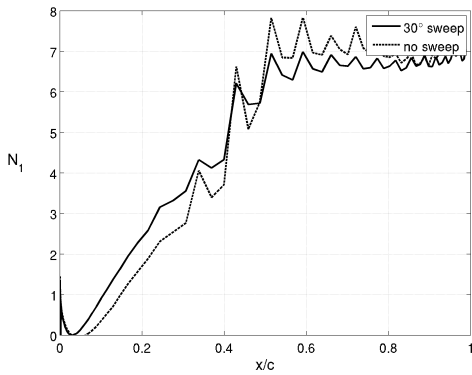
Figure 13. Amplification factor N_1 **of streamwise perturbations: comparison of un-swept and** $30°$ **sweep wing at** $Re_x = 60,000.$
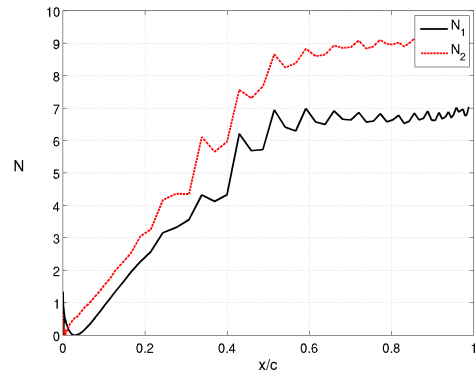
Figure 14. Streamwise and cross-flow amplification factors, N_1 **and** N_2 **respectively, for** $30°$ **sweep wing at** $Re_x = 60,000.$

American Institute of Aeronautics and Astronautics

a mixed result of streamwise and cross-flow disturbances. We shall come back to this important fact later.

With $\Lambda = 30°$, the cross-flow amplification factor N_2 has a similar slope (close to 15) in the linear-growth region to the streamwise amplification factor N_1, but a larger normalized magnitude at any given chord-wise location. However, this does not allow us to determine whether transition is caused by the growth of TS waves or by cross-flow disturbances: the threshold where transition occurs might not be the same for both amplification factors, and there is no currently known value of critical cross-flow amplification factor — the determination of an appropriate value being outside the scope of the present research, especially since the mechanism of cross-flow instability might not be as accurately reduced to the amplification of cross-flow disturbances as purely TS transition is.

V.   Effect of Sweep Angle

Having seen how the presence of cross-flow induced by a $30°$ sweep can accelerate transition, we now quantify how different sweep angles affect the boundary layer development by considering sweep angles $\Lambda \in \{0°, 1°, 5°, 10°, 20°, 30°, 40°, 50°, 60°\}$. The average results are summarized in Table 1.

A.   Forces

When normalizing the forces with respect to the chord-wise dynamic pressure, q_{∞_x}, there is little change in lift coefficient, C_{Lx}, which remains at 0.6 within about 5% for all sweep angles considered as illustrated in Figure 15 (blue line with triangles). Indeed, lift is primarily the result of pressure forces which, when normalized properly, change little with sweep angle and only in the region close to transition as can be seen in Figure 16. On the other hand, the drag coefficient, C_{Dx}, increases for sweep angles of $30°$ and more, probably due to the rise in friction coefficient associated with an earlier transition, as well as to some non-linear effects in the interaction between streamwise and cross-flow components. As expected, the third coefficient of force, C_{Cx}, (in the direction normal to both lift and drag) increases almost linearly with Λ.

If we now look at the lift and drag as commonly defined with respect to the free-stream (C_L and C_D black lines and circles of Figure 15), both lift and drag decrease close to linearly for moderate and large sweep angles ($\Lambda \geq 20°$) as occurs when a wing is swept and its profile is effectively elongated. It is interesting that the third force component increases and then decreases, having a maximum at around $\Lambda = 30°$; however, in a typical vehicle configuration with two symmetric wings, this lateral force would be counteracted by an equal and opposite one from the other wing and hence would have no impact on the overall aerodynamics of the vehicle.
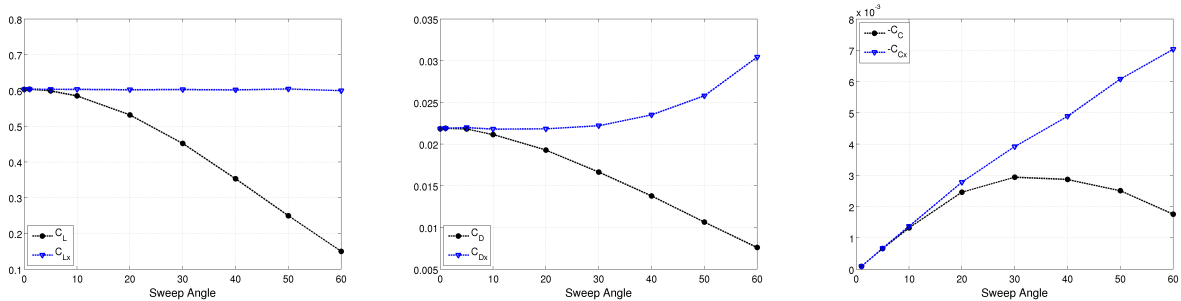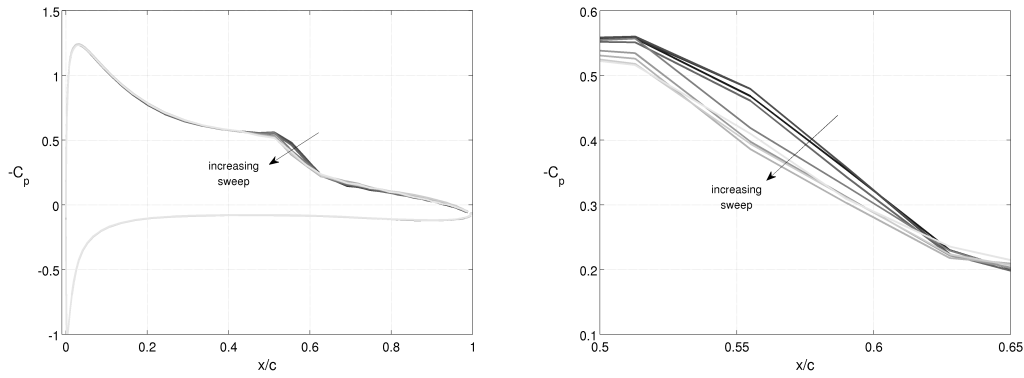

Figure 15.   Variation of force coefficients with sweep angle at $Re_x = 60,000$: lift coefficient (top left), drag coefficient (top right), and span-wise force coefficient (bottom); the subscript x refer to the force coefficients non-dimensionalized with respect to the chord-wise direction.

American Institute of Aeronautics and Astronautics

Table 1. Summary of average flow results for swept wings at $Re_x = 60,000$ and $4°$ angle of attack.

Sweep Angle	0°	1°	5°	10°	20°	30°	40°	50°	60°
C_L	0.6030	0.6036	0.5987	0.5849	0.5316	0.4519	0.3530	0.2496	0.1499
C_{Lx}		0.6038	0.6033	0.6031	0. 6021	0.6025	0.6015	0.6042	0.5994
C_D	0.02184	0.02190	0.02182	0.02114	0.01928	0.01665	0.01379	0.01065	0.00760
C_{Dx}		0.02191	0.02198	0.02179	0.02183	0.02220	0.02350	0.02579	0.03042
$-C_C$	-	0.00009	0.00066	0.00132	0.00246	0.00294	0.00287	0.00251	0.00176
$-C_{Cx}$		0.00009	0.00067	0.00137	0.00278	0.00392	0.00489	0.00608	0.00703
x_{sep}/c from C_{fx}	0.2365	0.2374	0.2360	0.2387	0.2431	0.2485	0.2515	0.2498	0.2460
x_{sep}/c from $H = 4$	0.2380	0.2390	0.2372	0.2404	0.2450	0.2483	0.2502	0.2492	0.2468
x_{tr}/c from H_{11}	0.4870	0.4870	0.4870	0.4586	0.4586	0.3996	0.3996	0.3996	0.3996
x_{tr}/c from H		0.4850	0.4980	0.4870	0.4710	0.4560	0.4560	0.4450	0.4470
x_r/c from C_{fx}	0.6121	0.6104	0.6107	0.6076	0.6008	0.5968	0.6009	0.6009	0.5939
x_r/c from $H = 4$	0.5637	0.5716	0.5703	0.5628	0.5566	0.5439	0.5372	0.5384	0.5470
max (H_{11})	7.4000	7.7418	7.2925	6.5602	5.8552	5.0812	4.6081	4.1548	3.7707
max (H)		7.7472	7.3756	6.7746	6.5794	6.2124	5.9570	5.8463	5.9160
max ($-\overline{u}_2/\overline{u}_e$) at $x/c = 0.1$	-	0.000538	0.002622	0.005189	0.010127	0.014651	0.018426	0.020914	0.020816
maximum x/c with $-\overline{u}_2 < 0$	0	0.0020	0.0787	0.1006	0.1139	0.1291	0.1291	0.1464	0.1291
$dN_1/d(x/c)$	13.16	14.81	12.42	12.62	15.74	16.06	14.67	16.58	12.59
$dN_2/d(x/c)$	-	13.07	7.20	8.12	14.27	15.11	9.73	12.97	9.15
N_1 at x_{tr}/c	6.3	5.9	5.5	5.7	5.9	4.4	4.4	4.6	4.3
N_2 at x_{tr}/c	-	10.4	8.8	8.5	8.1	6.8	6.2	6.5	5.7

American Institute of Aeronautics and Astronautics

Figure 16. Average pressure coefficient comparison of different sweep angles of $\{0°, 1°, 5°, 10°, 20°, 30°, 40°, 50°, 60°\}$ **at** $Re_x = 60,000$.
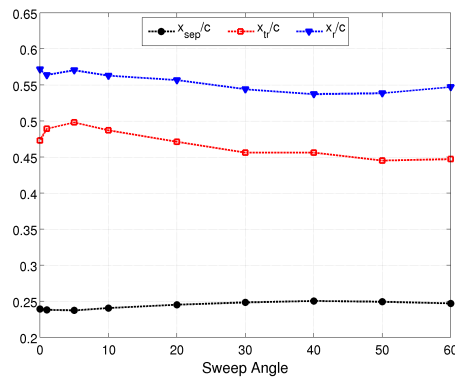
Figure 17. Variation of separation x_{sep}/c, transition x_{tr}/c, and reattachment x_r/c locations with sweep angle at $Re_x = 60,000$.

B. Separation, Transition, Reattachment

Separation occurs almost at the same chord-wise location across all sweep angles, as measured from the two-dimensional equivalent shape factor and the common location where $H = 4$. The earliest and latest separations are observed at 24% and 25% of the chord, respectively, showing that separation location varies only by about than 6% (moving upstream by less than 1.5% of the chord) even for sweep angles up to 60°, as illustrated in Figure 17.

The separation location is basically left unchanged since, for all sweep angles at these low Reynolds numbers, the boundary layer separates while being laminar and hence separation is determined by the chord-wise pressure gradient. The presence of more or less cross-flow at the different sweep angles influences the growth of disturbances, but has no effect on the laminar boundary layer development and separation.

On the contrary, transition does vary significantly with sweep angle as can be readily observed in the pressure coefficient on the wing's upper surface shown in Figure 16. Transition location is determined by computing the boundary layer two-dimensional equivalent shape factor H (Figure 21) and measuring its peak. Transition takes place between $0.445c$ and 0.498, a close to 12% difference, and for $\Lambda \geq 5°$ moves farther and farther upstream (by as much as 5% of the chord) as the sweep angle is increased.

The reattachment location is more accurately measured as the place where the shape factor H goes back down to a value of 4 after transition — since the friction coefficient is not a good measure of the flow nature, especially aft of separation. Transition occurring earlier for larger sweep angles, the flow reattaches faster as expected. Reattachment takes place as late as $x_r/c = 0.5716$ for the un-swept wing, but moves up to $0.5372c$ for $\Lambda = 40°$: reattachment is pushed upstream by as much as 3.5% of the chord. This represents a difference of only 6% while transition between these two cases moves upstream by 12%; this is to be explained by the fact that turbulent flow fluctuations do create more momentum but not all of the momentum gain is readily

American Institute of Aeronautics and Astronautics

organized into a shear layer shape that induces reattachment.

To summarize, the change in transition location (by up to $0.05c$) is more significant than the change in both separation (up to $0.015c$) and reattachment (up to $0.035c$) locations: transition is dominated by the growth of unstable perturbations and hence strongly influenced by the presence of a destabilizing cross-flow, while laminar separation is set by the pressure gradient which is left unchanged in the chord-wise direction. Reattachment (influenced both by the unchanged pressure gradient and the transition) does globally move upstream due to the faster transition, thus making the laminar separation bubble shorter.

It is important to note that the uncertainly in determining the relevant locations is not insignificant, especially at small sweep angles. In particular, transition is taken at the location of the peak in the two-dimensional equivalent shape factor, and the peak region is not smooth given the relative coarseness of the grid employed.

C. Boundary Layer

The plots of streamwise boundary layer displacement thickness, momentum thickness, and shape factor of Figure 19 show a continuous change in boundary layer shape — except for the case at $\Lambda = 1°$ — as the sweep angle is increased: the peak in H_{11} moves upstream and its maximum value decreases as quantified in Figure 18. Even a small sweep angle of $\Lambda = 10°$ (which induces only little cross-flow and small cross-flow perturbations) is enough to change the stability characteristics of the streamwise boundary layer profile, as evidenced now by the change (about 13%) in $\max(H_{11})$ between $0°$ and $10°$. As the sweep angle is increased further, the maximum shape factor continues to decrease but at a lower and lower rate.

The cross-flow displacement thickness becomes larger and larger at any chord-wise location when the sweep angles increases as can be seen in Figure 20: larger sweep angles generate more cross-flow and hence a larger δ_2^* as from equation (G).

As mentioned earlier, since the chord-wise characteristics are constant across all sweeps (same airfoil profile, angle of attack, chord-wise Reynolds number) the two-dimensional-equivalent quantities δ^*, θ, H can provide a meaningful comparison by decoupling the cross-flow components from the purely chord-wise boundary layer evolution. In other words, if the cross-flow and streamwise effects are only linearly coupled, the curves for different sweep angles should collapse into a single line.

Comparing the plots of δ^*, θ, H in Figure 21 clearly demonstrates that the span-wise/cross-flow effects cannot be considered independently of the chord-wise/streamwise evolution for sweep angles between $10°$ and $30°$: the influence of the latter on the former is non-linear. On the other hand, for $\Lambda = 1°$ and $\Lambda = 5°$, the two-dimensional equivalent boundary layer curves collapse, indicating that only linear interactions occur; the same happens for sweep angles of $40°$ and larger.

These are evident in most of the curves presented next, as well as on Figure 18 which shows the maximum in H: if we ignore the $\Lambda = 1°$ point, the curve is flat between $0°$ and $5°$ sweep, and then again for $\Lambda \geq 40°$. In between, the interaction between cross-flow and streamwise components is non-linear and there is a continuous decrease in the H peak as the sweep angle is increased.
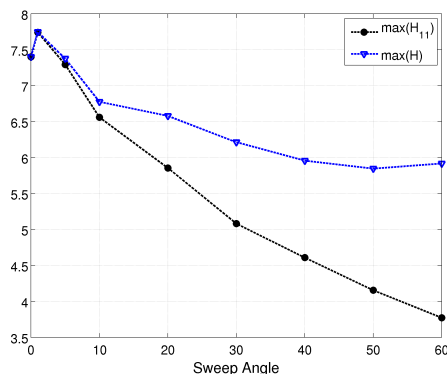
Figure 18. Variation of boundary layer streamwise shape factor maximum, $\max(H_{11})$, and two-dimensional equivalent shape factor maximum, $\max(H)$, with sweep angle at $Re_x = 60,000$.
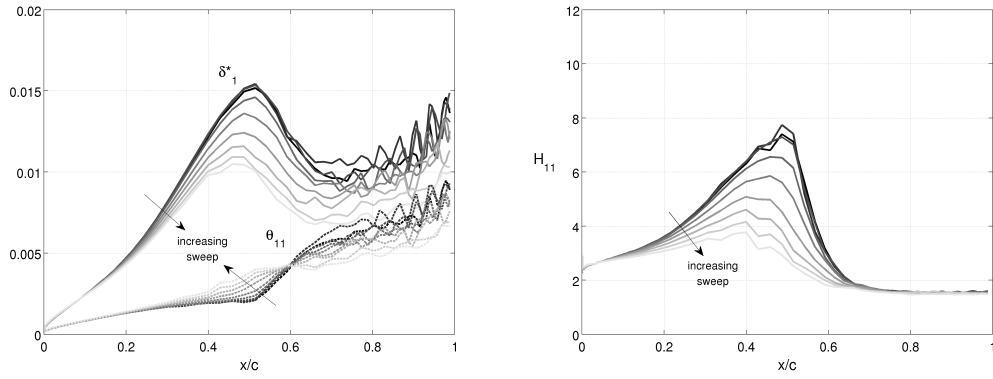
American Institute of Aeronautics and Astronautics

Figure 19. Boundary layer average streamwise displacement and momentum thicknesses (left), and shape factor (right) evolution for sweep angles of $\{0°, 1°, 5°, 10°, 20°, 30°, 40°, 50°, 60°\}$ **at** $Re_x = 60,000$.
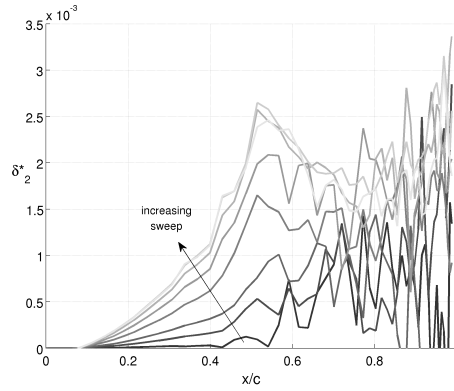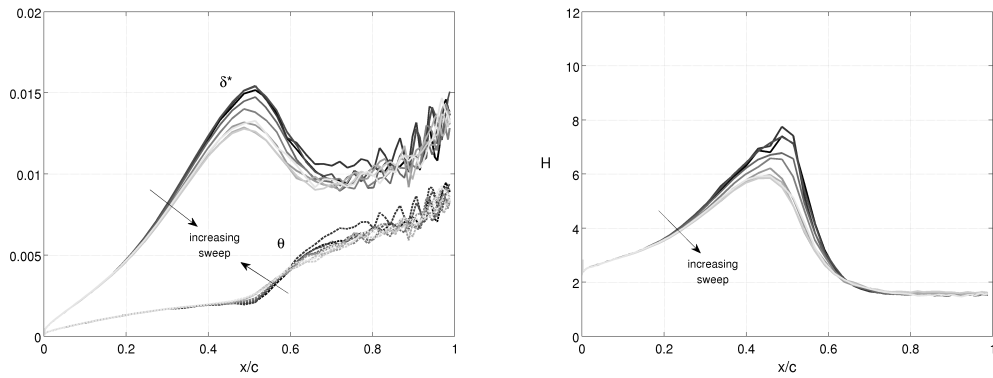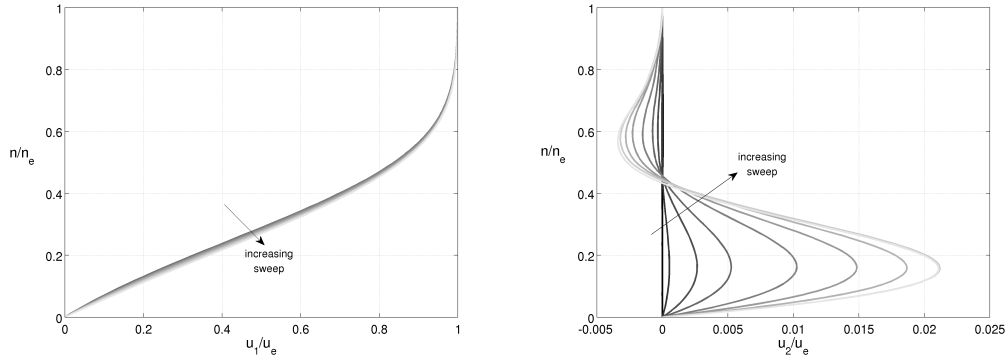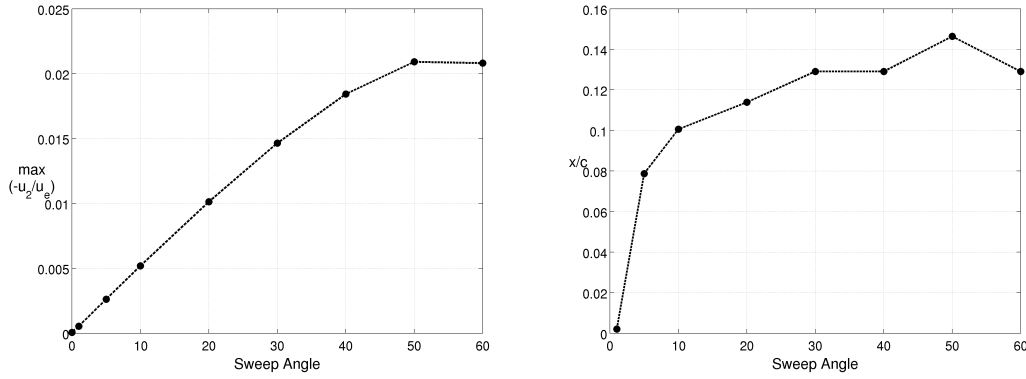

Figure 20. Boundary layer average cross-flow displacement thickness evolution for sweep angles of $\{0°, 1°, 5°, 10°, 20°, 30°, 40°, 50°, 60°\}$ **at** $Re_x = 60,000$.

Figure 21. Boundary layer average equivalent chord-wise displacement and momentum thicknesses (left), and shape factor (right) evolution for sweep angles of $\{0°, 1°, 5°, 10°, 20°, 30°, 40°, 50°, 60°\}$ **at** $Re_x = 60,000$.

American Institute of Aeronautics and Astronautics

Figure 22. Boundary layer average profiles of streamwise $\overline{u}_1/\overline{u_e}$ (right) and cross-flow pseudo-velocity $-\overline{u}_2/\overline{u_e}$ (left) at $x/c \in [0.1, 0.15]$ for sweep angles of $\{0°, 5°, 10°, 20°, 30°, 40°, 50°, 60°\}$ at $Re_x = 60,000$.

Figure 23. Variation of the average boundary layer cross-flow pseudo-velocity profile $-\overline{u}_2/\overline{u}_e$ characteristics with sweep angle at $Re_x = 60,000$: maximum at $x/c = 0.1$ (left) and chord-wise location where the profile stops being S-shaped, that is where $\min(\overline{u}_2/\overline{u}_e) \geq 0$ (right).

In the laminar region, all the curves of two-dimensional equivalent boundary layer integral quantities overlap: if the cross-flow affects streamwise disturbances, these play no role in the laminar boundary layer development. Once separation occurs, the disturbances are rapidly amplified and the interactions become highly non-linear: the largest difference between the curves occurs around the transition region where disturbance growth and their interactions dominate the shear layer evolution.

Note that the curves of boundary layer quantities at $0°$ and $1°$ sweep in Figures 19 and 21 are not smooth near transition. This can be attributed to the coarseness of the grids being used and to the very high sensitivity of boundary layer quantities near transition to spatial resolution. Furthermore, the uncertainty in determining the separation, transition, and reattachment locations shows in Figure 17 is relatively large. Therefore, while we believe the major trends discussed in this section can be trusted, the exact values could benefit from a more accurate solution; this is particularly true at certain sweep angles ($0°$ and $1°$ certainly, and probably also $10°$) and it is thus not possible to draw some conclusions with confidence.

As the average streamwise and cross-flow pseudo-velocity profiles of Figure 22 show, the streamwise flow is only slightly modified but the cross-flow component sees significant changes with varying sweep angle. In particular, the value of the maximum cross-flow velocity at any given chord-wise location, *e.g.* at $x/c = 0.1$ as in the plots on the left of Figure 22, increases while its minimum decreases when Λ increases. This is similar to what happens when moving downstream in the chord-wise direction: the cross-flow profiles becomes more and more unstable as we either move downstream or increase the sweep angle. Again, this verifies that the presence of cross-flow has a destabilizing effect.

From the the precise variation of maximum cross-flow velocity with sweep angle at $x/c = 0.1$ of Figure 23, it can be noted that the maximum cross-flow value increases linearly up to about $\Lambda = 40°$ before starting to level off. This saturation suggests that increasing the sweep cannot result in an arbitrarily large cross-flow.

Similarly, there seems to be a limit of how far downstream cross-flow S-shaped profiles (*i.e.* with two-

American Institute of Aeronautics and Astronautics

inflection points) can exist, all the profiles having a single inflection point far enough downstream — even long before separation. As the left plot of Figure 23 shows, S-shaped profiles are present in longer and longer regions near the leading edge as the sweep angle is increased, but their spatial extent does not seem to increase above about $0.14c$ when the curve levels off for $\Lambda \geq 30°$.

D. Amplification Factors

The streamwise and cross-flow amplification factors, N_1 and N_2, for different sweep angles can be seen in Figure 24. Contrarily to the average boundary layer integral quantities, the change in amplification factors is not uniform with sweep angle: the growth (even linear) of disturbances is more complex than the average boundary layer development, and a simple correlation seems unlikely. However, this hypothesis needs to be verified with better resolved simulations, as the average results at some of the sweep angles are particularly noisy.

Correspondingly, the slopes of streamwise and cross-flow amplification factors in their linear regions vary non-uniformly with sweep angle as quantified in Figure 25. The linear slope of N_1 varies by as much as 30% with sweep angle, and an even larger change is observed in the growth of the cross-flow disturbances which almost doubles from $\Lambda = 5°$ to $\Lambda = 20°$. What happens for sweep angles larger than 30° (slope amplitudes decrease, then increase, and then increase again) can be interpreted as the effect of a complex interaction between streamwise and cross-flow unstable waves.

Figure 26 shows the values of N_1 and N_2 at transition for the different sweeps. If transition were due to cross-flow instabilities for $\Lambda = 60°$ (which is the most likely candidate for cross-flow transition), then transition would also have to be caused by cross-flow instabilities at all the other sweep angles since they all
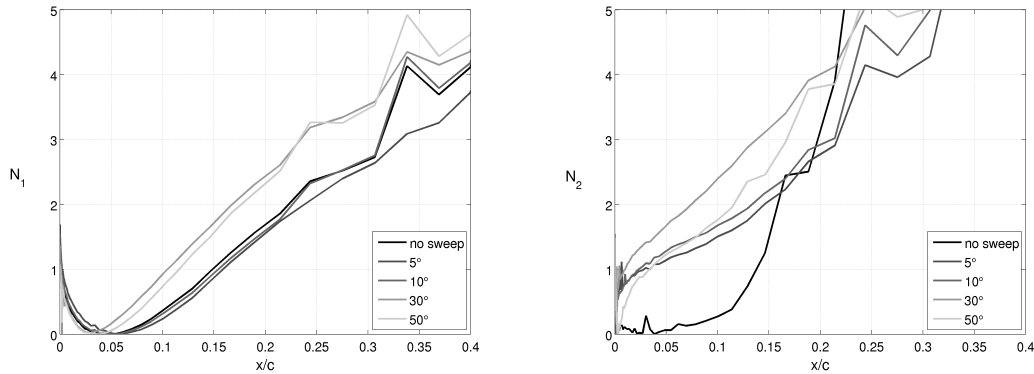

Figure 24. Streamwise amplification factor N_1 (left), and cross-flow amplification factor N_2 (right): comparison of different sweep angles at $Re_x = 60,000$.
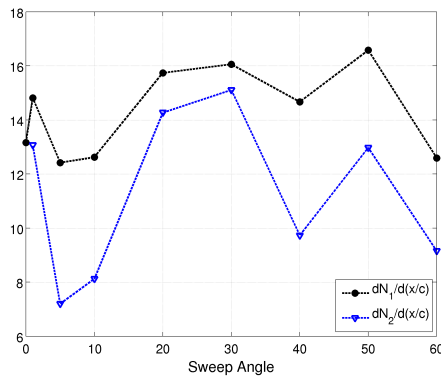

Figure 25. Variation of streamwise and cross-flow amplification factor slopes in the linear-growth region, $dN_1/d(x/c)$ and $dN_2/d(x/c)$, with sweep angle at $Re_x = 60,000$.
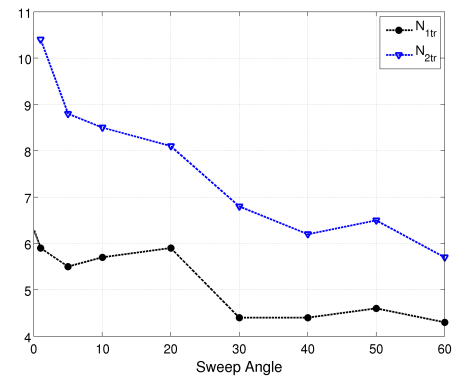
Figure 26. Variation of streamwise and cross-flow amplification factor at transition with sweep angle at $Re_x = 60,000$.

American Institute of Aeronautics and Astronautics

have a value of N_2 at transition lower than that for $\Lambda = 60°$ — of course assuming that there is a critical cross-flow amplification analog to the critical amplification factor in two-dimensional flows. However, it seems unlikely that transition at such a small sweep angle as 5° would be the result of unstable cross-flow disturbances. Therefore, the following hypothesis seems again the most plausible: transition over the swept wing at this low Reynolds number is caused by the growth of unstable TS waves (just as it was for the unswept wing), but the presence of even small cross-flow velocities destabilizes the laminar streamwise profile and accelerates transition; in other words, we are in the presence of a mixed transition at intermediate sweep angles.

Again, at this point it is not possible to determine at which critical cross-flow amplification factor transition can be assumed to occur, and hence it is even harder to determine which type of disturbance (TS or cross-flow waves) is eventually responsible for transition. However, for sweep angles of 30° and more, the value of N_1 at transition remains more or less constant close to 5.5, while transition location keeps moving upstream: this suggest that transition at large sweeps is primarily dominated by cross-flow disturbances. In spite of this, N_2 at transition keeps decreasing; one should remember at this point that cross-flow transition may not be characterized by solely the linear growth of disturbances, as can often be done for TS-dominated transition.

VI.   Summary and Conclusions

Very little being known about the influence of cross-flow on transition at low Reynolds numbers, a preliminary numerical study of the flow around an infinite SD7003 wing at low Reynolds number and various sweep angles has been presented. While keeping the chord-wise Reynolds number, angle of attack, and SD7003 geometry constant, the effects of cross-flow are determined by projecting the boundary layer velocity components along the relevant two-dimensional equivalent directions. In this way, if the cross-flow and streamwise components were only linearly coupled, curves for different sweep angles would collapse into a single line.

Three facts observed throughout this preliminary investigation of the effects of cross-flow on transition are worth emphasizing. One is the saturation phenomena observed at large sweep angles: after "enough" cross-flow is present (a fuzzy threshold), the flow becomes somewhat insensitive to further increases, and the cross-flow stops being strongly influential even before the sweep angle becomes inefficient in generating cross-flow. This is seen in many of the curves which flatten-out for large values of Λ, *e.g.* maximum in H and transition location.

Second, the streamwise and cross-flow components cannot be decoupled from a stability point of view for intermediate sweep angles (roughly between $\Lambda = 10°$ and 40°) and the resulting mixed transition is due to the presence of strong non-linear interactions. Considering the two components independently is however possible for either very small or very large sweep angles. This is consistent with the high Reynolds number observations[7] and reports which have successfully decoupled them.[6]

Finally, even a small amount of cross-flow can significantly affect transition, as evidenced by the large changes between results at 0° and 10° sweep. Transition and turbulence are highly non-linear processes, and the stability characteristics of boundary and shear layers are very sensitive to even small perturbation. An important consequence is that, at these low Reynolds numbers in which transition takes place along a laminar separation bubble, a purely TS-wave based transition is unlikely to be successful in real flow conditions since the free-stream is unlikely to be (nor to stay) purely in the chord-wise direction. This misalignment is more pronounced on instantaneous fields and with flapping vehicles, and more so at low than high Reynolds numbers due to the low inertia of the flow. An important presumption to be adopted in the study of MAVs and animal locomotion is thus that the type of transition (TS dominated, cross-flow dominated, or mixed) is *a priori* unknown.

The use of an Implicit Large Eddy Simulation (ILES) with a Discontinuous Galerkin (DG) method has again[2,3] proven to be appropriate at predicting the flows involved. However, due to the coarseness of the computational grid employed, it is not yet possible to conclude with full confidence. We are presently validating these results by performing higher-resolved simulations in order to reduce the uncertainty of the trends observed here, as well as validate or disprove some of the hypothesis presented. An update will follow shortly in a future publication.

Acknowledgments

References

[1] Uranga, A., Persson, P.-O., Drela, M., and Peraire, J., "Implicit Large Eddy Simulation of transitional flows over airfoils and wings," *19th AIAA Computational Fluid Dynamics Conference, June 22-25, 2009, San Antonio, TX, AIAA-2009-4131*, 2009.

[2] Uranga, A., Persson, P.-O., Drela, M., and Peraire, J., "Implicit Large Eddy Simulation of transition to turbulence at low Reynolds numbers using a Discontinuous Galerkin method," *International Journal for Numerical Methods in Engineering*, Vol. 87, No. 1-5, 2011, pp. 232–261.

[3] Uranga, A., *Investigation of transition to turbulence at low Reynolds numbers using Implicit Large Eddy Simulations with a Discontinuous Galerkin method*, Ph.D. thesis, Massachusetts Institute of Technology, Cambridge, MA, 2011.

[4] Reed, H. and Saric, W., "Stability of three-dimensional boundary layers," *Annual Review of Fluid Mechanics*, Vol. 21, 1989, pp. 235–284.

[5] Reed, H. and Saric, W., "Linear stability theory applied to boundary layers," *Annual Review of Fluid Mechanics*, Vol. 28, 1996, pp. 389–428.

[6] Reshotko, E., "Boundary layer instability, transition and control," *32nd AIAA Aerospace Sciences Meeting and Exhibit, Jan. 10-13, 1994, Reno, NV, AIAA-94-0001*, 1994.

[7] Strokowsky, A. and Orszag, S., "Mass flow requirements for LFC wing design," *AIAA Aircraft Systems and Technology Meeting, Seattle, WA, Aug. 22-24*, 1977.

[8] Arnal, D., "Predictions based on linear theory," *AGARD Report No. 793*, 1994.

[9] Saric, W., Reed, H., and White, E., "Stability and transition of three-dimensional boundary layers," *Annual Review of Fluid Mechanics*, Vol. 35, 2003, pp. 413–440.

[10] Roe, P. L., "Approximate Riemann solvers, parameter vectors, and difference schemes," *J. Comput. Phys.*, Vol. 43, No. 1, 1981, pp. 357–372.

[11] Peraire, J. and Persson, P.-O., "The Compact Discontinuous Galerkin (CDG) method for elliptic problems," *SIAM Journal of Scientific Computing*, Vol. 30, No. 4, 2008, pp. 1806–1824.

[12] Persson, P.-O. and Peraire, J., "Newton-GMRES preconditioning for Discontinuous Galerkin discretizations of the Navier-Stokes equations," *SIAM Journal of Scientific Computing*, Vol. 30, No. 6, 2008, pp. 2709–2733.

[13] Persson, P.-O., "Scalable parallel Newton-Krylov solvers for Discontinuous Galerkin discretizations," *Proc. of the 47th AIAA Aerospace Sciences Meeting and Exhibit, Reno, Nevada, AIAA-2009-606*, 2009.

[14] Galbraith, M. and Visbal, M., "Implicit Large-Eddy Simulation of low Reynolds number flow past the SD7003 airfoil," *46th AIAA Aerospace Sciences Meeting and Exhibit, Jan. 7-10, 2008, Reno, NV, AIAA-2008-225*, 2008.

[15] Visbal, M., Gordnier, R., and Galbraith, M., "High-fidelity simulations of moving and flexible airfoils at low Reynolds numbers," *Experiments in Fluids*, Vol. 46, 2009, pp. 903–922.

[16] Garmann, D. and Visbal, M., "High-fidelity simulations of transitional flow over pitching airfoils," *39th AIAA Fluid Dynamics Conference, June 22-25, 2009, San Antonio, TX, AIAA-2009-3693*, 2009.

[17] Visbal, M., "High-fidelity simulation of transitional flows past a plunging airfoil," *47th AIAA Aerospace Sciences Meeting, Jan. 5-8, 2009, Orlando, FL, AIAA-2009-391*, 2009.

[18] Alexander, R., "Diagonally Implicit Runge-Kutta methods for stiff O.D.E.'s," *SIAM J. Numer. Anal.*, Vol. 14, No. 6, 1977, pp. 1006–1021.

[19] Dubeif, Y. and Delcayre, F., "On Coherent-vortex Identification in Turbulence," *Journal of Turbulence*, Vol. 1, No. 11, 2000, pp. 1–22.

[20] Galbraith, M. and Visbal, M., "Implicit Large Eddy Simulaion of low Reynolds number flow past the SD7003 airfoil," *Proc. of the 46th AIAA Aerospace Sciences Meeting and Exhibit, Reno, Nevada, AIAA-2008-225*, 2008.